The Astrophysical Journal Letters, 945:L10 (13pp), 2023 March 1 https://doi.org/10.3847/2041-8213/acacfb

First Look at $z > 1$ Bars in the Rest-frame Near-infrared with JWST Early CEERS Imaging

Yuchen Guo[1], Shardha Jogee[1], Steven L. Finkelstein[1], Zilei Chen[1], Eden Wise[1], Micaela B. Bagley[1], Guillermo Barro[2], Stijn Wuyts[3], Dale D. Kocevski[4], Jeyhan S. Kartaltepe[5], Elizabeth J. McGrath[4], Henry C. Ferguson[6], Bahram Mobasher[7], Mauro Giavalisco[8], Ray A. Lucas[6], Jorge A. Zavala[9], Jennifer M. Lotz[10], Norman A. Grogin[6], Marc Huertas-Company[11,12,13], Jesús Vega-Ferrero[11], Nimish P. Hathi[6], Pablo Arrabal Haro[14], Mark Dickinson[14], Anton M. Koekemoer[6], Casey Papovich[15,16], Nor Pirzkal[17], L. Y. Aaron Yung[18,34], Bren E. Backhaus[19], Eric F. Bell[20], Antonello Calabrò[21], Nikko J. Cleri[15,16], Rosemary T. Coogan[22], M. C. Cooper[23], Luca Costantin[24], Darren Croton[25,26], Kelcey Davis[27], Avishai Dekel[28], Maximilien Franco[1], Jonathan P. Gardner[18], Benne W. Holwerda[29], Taylor A. Hutchison[18,35], Viraj Pandya[30,36], Pablo G. Pérez-González[31], Swara Ravindranath[6], Caitlin Rose[5], Jonathan R. Trump[19], Alexander de la Vega[32], and Weichen Wang[33]

[1] Department of Astronomy, The University of Texas at Austin, Austin, TX, USA
[2] Department of Physics, University of the Pacific, Stockton, CA 90340, USA
[3] Department of Physics, University of Bath, Claverton Down, Bath BA2 7AY, UK
[4] Department of Physics and Astronomy, Colby College, Waterville, ME 04901, USA
[5] Laboratory for Multiwavelength Astrophysics, School of Physics and Astronomy, Rochester Institute of Technology, 84 Lomb Memorial Drive, Rochester, NY 14623, USA
[6] Space Telescope Science Institute, 3700 San Martin Drive, Baltimore, MD 21218, USA
[7] Department of Physics and Astronomy, University of California, 900 University Avenue, Riverside, CA 92521, USA
[8] University of Massachusetts Amherst, 710 North Pleasant Street, Amherst, MA 01003-9305, USA
[9] National Astronomical Observatory of Japan, 2-21-1 Osawa, Mitaka, Tokyo 181-8588, Japan
[10] Gemini Observatory/NSF's National Optical-Infrared Astronomy Research Laboratory, 950 N. Cherry Avenue, Tucson, AZ 85719, USA
[11] Instituto de Astrofísica de Canarias, La Laguna, Tenerife, Spain
[12] Universidad de la Laguna, La Laguna, Tenerife, Spain
[13] Université Paris-Cité, LERMA—Observatoire de Paris, PSL, Paris, France
[14] NSF's National Optical-Infrared Astronomy Research Laboratory, 950 N. Cherry Avenue, Tucson, AZ 85719, USA
[15] Department of Physics and Astronomy, Texas A&M University, College Station, TX 77843-4242 USA
[16] George P. and Cynthia Woods Mitchell Institute for Fundamental Physics and Astronomy, Texas A&M University, College Station, TX 77843-4242 USA
[17] ESA/AURA Space Telescope Science Institute, 3700 San Martin Drive, Baltimore, MD, 21218, USA
[18] Astrophysics Science Division, NASA Goddard Space Flight Center, 8800 Greenbelt Road, Greenbelt, MD 20771, USA
[19] Department of Physics, University of Connecticut, 196A Auditorium Road, Unit 3046, Storrs, CT 06269, USA
[20] Department of Astronomy, University of Michigan, 1085 S. University Avenue, Ann Arbor, MI 48109-1107, USA
[21] INAF Osservatorio Astronomico di Roma, Via Frascati 33, I-00078 Monteporzio Catone, Rome, Italy
[22] CEA, IRFU, DAp, AIM, Université Paris-Saclay, Université Paris Cité, Sorbonne Paris Cité, CNRS, F-91191 Gif-sur-Yvette, France
[23] Department of Physics & Astronomy, University of California, Irvine, 4129 Reines Hall, Irvine, CA 92697, USA
[24] Centro de Astrobiología (CSIC-INTA), Ctra de Ajalvir km 4, Torrejón de Ardoz, E-28850 Madrid, Spain
[25] Centre for Astrophysics & Supercomputing, Swinburne University of Technology, Hawthorn, VIC 3122, Australia
[26] ARC Centre of Excellence for All Sky Astrophysics in 3 Dimensions (ASTRO 3D), Australia
[27] Department of Physics, University of Connecticut, 196 Auditorium Road, Unit 3046, Storrs, CT 06269, USA
[28] Racah Institute of Physics, The Hebrew University of Jerusalem, Jerusalem 91904, Israel
[29] Physics & Astronomy Department, University of Louisville, Louisville, KY 40292, USA
[30] Columbia Astrophysics Laboratory, Columbia University, 550 West 120th Street, New York, NY 10027, USA
[31] Centro de Astrobiología (CAB), CSIC-INTA, Ctra. de Ajalvir km 4, Torrejón de Ardoz, E-28850 Madrid, Spain
[32] Department of Physics and Astronomy, University of California, Riverside, CA 92521, USA
[33] Department of Physics and Astronomy, Johns Hopkins University, 3400 N. Charles Street, Baltimore, MD 21218, USA
Received 2022 October 14; revised 2022 December 10; accepted 2022 December 11; published 2023 March 1

Abstract

Stellar bars are key drivers of secular evolution in galaxies and can be effectively studied using rest-frame near-infrared (NIR) images, which trace the underlying stellar mass and are less impacted by dust and star formation than rest-frame UV or optical images. We leverage the power of JWST CEERS NIRCam images to present the first quantitative identification and characterization of stellar bars at $z > 1$ based on rest-frame NIR F444W images of high resolution ($\sim$1.3 kpc at $z \sim 1$–3). We identify stellar bars in these images using quantitative criteria based on ellipse fits. For this pilot study, we present six examples of robustly identified bars at $z > 1$ with spectroscopic redshifts, including the two highest-redshift bars at $z \sim 2.136$ and 2.312 quantitatively identified and characterized

[34] NASA Postdoctoral Fellow.
[35] NASA Postdoctoral Fellow.
[36] Hubble Fellow.

to date. The stellar bars at $z \sim 1.1$–2.3 presented in our study have projected semimajor axes of ∼2.9–4.3 kpc and projected ellipticities of ∼0.41–0.53 in the rest-frame NIR. The barred host galaxies have stellar masses $\sim 1 \times 10^{10}$ to $2 \times 10^{11}\ M_{\odot}$ and star formation rates of ∼21–295 $M_{\odot}\ \mathrm{yr}^{-1}$, and several have potential nearby companions. Our finding of bars at $z \sim 1.1$–2.3 demonstrates the early onset of such instabilities and supports simulations where bars form early in massive dynamically cold disks. It also suggests that if these bars at lookback times of 8–11 Gyr survive out to present epochs, bar-driven secular processes may operate over a long time and have a significant impact on some galaxies by $z \sim 0$.

Unified Astronomy Thesaurus concepts: Galaxy bars (2364); Barred spiral galaxies (136); Galaxy structure (622); Galaxy evolution (594)

1. Introduction

Stellar bars play a central role in the secular evolution of galaxies by efficiently redistributing mass and angular momentum and driving gas inflows into the circumnuclear region through gravitational torques and shocks (e.g., Athanassoula 2002; Kormendy & Kennicutt 2004; Athanassoula 2005; Jogee et al. 2005). Most present-day spirals are barred (e.g., Eskridge et al. 2000; Laurikainen et al. 2004; Marinova & Jogee 2007; Menéndez-Delmestre et al. 2007), including our own Milky Way (Petters 1975; Blitz & Spergel 1991; Binney et al. 1991; Weiland et al. 1994).

Observational evidence in nearby galaxies suggests bars influence their central molecular gas concentrations (e.g., Sakamoto et al. 1999; Jogee et al. 2005), velocity fields of ionized gas (e.g., Regan et al. 1997), star formation (SF) activity (e.g., Hunt & Malkan 1999; Jogee et al. 2005; Masters et al. 2010; George et al. 2021), and central bulges (e.g., Kormendy & Kennicutt 2004; Jogee et al. 2005; Gadotti 2011). The role of bars on active galactic nuclei (AGN) is less clear as both simulations (e.g., Combes & Gerin 1985; Athanassoula 1992a) and observations (e.g., Knapen et al. 1995; Buta & Combes 1996; Jogee et al. 2005) show that bar-driven gas inflows tend to stall in the circumnuclear region where the specific angular momentum of the gas is still too high to fuel the AGN (Jogee 2006).

The exploration of stellar bars out to early cosmic times is important for understanding the growth and morphological transformation of galaxies, a process that is driven since $z \sim 4$ by gas accretion (e.g., Katz et al. 2003; Kereš et al. 2005; Dekel & Birnboim 2006; Faucher-Giguère & Keres 2011; Kereš et al. 2012), galaxy mergers and tidal interactions (e.g., Conselice et al. 2003; Kartaltepe et al. 2007; Jogee et al. 2009; Lotz et al. 2010), as well as bar-driven secular processes. Numerous studies show near-infrared (NIR) images are better tracers than optical images of the stellar mass distribution and structural components of galaxies as the effects of dust extinction and SF are lower in the NIR (e.g., Frogel et al. 1996; Suess et al. 2022), and the mass-to-light ratio in the NIR is less sensitive to the ages of the stellar populations (e.g., Schneider 2006). Indeed, the bar fraction in bright spirals at $z \sim 0$ is higher in the NIR (e.g., Marinova & Jogee 2007; Menéndez-Delmestre et al. 2007) than in the optical. However, to date, studies of bars out to $z \sim 1$ have only been able to use the rest-frame optical light traced by Hubble Space Telescope (HST) WFPC2, Advanced Camera for Surveys (ACS), NICMOS, and WFC3 images.

Early HST studies of bars in the rest-frame optical by Elmegreen et al. (2004) and Jogee et al. (2004) presented the first evidence of a significant population of barred galaxies out to $z \sim 1$ (lookback time of ∼8 Gyr), showing that bars are already in place at early times and implying that bar-driven secular processes can potentially operate over many billions of years if these bars survive to the present day. Results on how the bar fraction varies out to $z \sim 1$ have been mixed: some studies (e.g., Elmegreen et al. 2004; Jogee et al. 2004) do not find a strong decline in the bar fraction out to $z \sim 1$, other studies find a decline by a factor of a few (e.g., Sheth et al. 2008; Melvin et al. 2014), while Cameron et al. (2010) point out that results on the bar fraction depend on the stellar mass range.

The vast majority of HST studies have explored bars in the rest-frame optical light out to $z \sim 1.2$ (e.g., Abraham et al. 1999; Elmegreen et al. 2004; Jogee et al. 2004; Sheth et al. 2008; Cameron et al. 2010; Melvin et al. 2014). The study by Simmons et al. (2014) represented a first attempt to push the explorations of bars in the rest-frame optical out to $z \leqslant 2$, but faced challenges in robustly characterizing bars at $z > 1.5$.

The advent of sensitive, high-resolution NIRCam images from the James Webb Space Telescope (JWST; Gardner et al. 2006) holds the promise of tremendous advances in the exploration of bars at $z > 1$ and provides us for the first time with high-resolution rest-frame NIR images at $z > 1$. At the same time, new high-resolution cosmological simulations (e.g., Kraljic et al. 2012; Scannapieco & Athanassoula 2012; Bonoli et al. 2016; Algorry et al. 2017; Spinoso et al. 2017; Fragkoudi et al. 2021; Rosas-Guevara et al. 2020, 2022; Bi et al. 2022) are probing the growth of bars and their impact on galaxy evolution out to $z \geqslant 4$.

In this pilot study we conduct the first quantitative exploration of stellar bars at $z > 1$ in high-resolution rest-frame NIR images by analyzing JWST NIRCam images in the first epoch of imaging from the Cosmic Evolution Early Release Science Survey (CEERS; Finkelstein et al. 2022). Thanks to the JWST F444W images, we can for the first time use high-resolution (0.″16 corresponding to ∼1.3 kpc at $z \sim 1$–3) rest-frame NIR images to quantitatively identify and characterize bars at $z > 1$. The sample selection is outlined in Section 3. In Section 4 we describe our methodology to identify and characterize bars based on the application of physically motivated quantitative criteria to ellipse fits. For this pilot study, we present in Section 5 six examples of robustly identified bars at $z > 1$ with spectroscopic redshifts, including the two highest-redshift bars at $z \sim 2.136$ and 2.312 quantitatively identified and characterized to date. Section 6 discusses the implications of our results for the onset and impact of early generations of bars on galaxy evolution.

We stress that this pilot study only presents six examples of robustly identified bars at $z > 1$ in the rest-frame NIR rather than a full census of all observable bars at $z > 1$. In future papers that will incorporate the upcoming additional six CEERS pointings, we will present such a full census of observable bars at $z > 1$, estimate the rest-frame optical and NIR bar fraction, and explore the relationship between bars and

galaxy properties (SF, bulges, AGN, and the presence of companions) using a control sample of unbarred galaxies.

In this Letter we assume the latest Planck flat ΛCDM cosmology with $H_0 = 67.36$, $\Omega_m = 0.3153$, and $\Omega_\Lambda = 0.6847$ (Planck Collaboration et al. 2020). All magnitudes are in the absolute bolometric system (AB; Oke & Gunn 1983).

2. CEERS Observations and Data Reduction

CEERS is one of 13 early release science surveys designed to obtain data covering all areas of astronomy early in Cycle 1. In this pilot Letter we use the first epoch of CEERS NIRCam imaging, which has 4 of the planned 10 pointings obtained on 2022 June 21, known as CEERS1, CEERS2, CEERS3, and CEERS6. We refer the reader to the CEERS survey (Finkelstein et al. 2022) and data reduction (Bagley et al. 2022) papers for a full description of the CEERS survey and briefly summarize the key aspects here. Data were obtained in each pointing in the short-wavelength (SW) channel F115W, F150W, and F200W filters, and long-wavelength (LW) channel F277W, F356W, F410M, and F444W filters with a typical exposure time of 2835 s per filter in each of three dithers, except for F115W, which had longer exposure times. A careful initial reduction of the NIRCam images in all four pointings was performed using version 1.5.3 of the JWST Calibration Pipeline[37] with some custom modifications. Version v0.07 of the CEERS data reduction was used in this work. As described in Finkelstein et al. (2022), data were processed through Stages 1 and 2 of the pipeline where reduction steps included detector-level correction, wisp subtraction, removal of *1/f* noise, flat-fielding, and masking of bad pixels. This was followed by astrometric correction and coaddition of calibrated detector images onto a common output grid using the drizzle algorithm with an inverse-variance map weighting (Casertano et al. 2000; Fruchter & Hook 2002). The rms of the absolute alignment to HST F160W is ∼12–15 mas, and the rms of the NIRCam-to-NIRCam alignment is ∼5–10 mas. The output mosaics have pixel scales of $0\farcs03$ pixel^{-1}. The usable total area covered by these observations is 34.5 arcmin^2. As described in Finkelstein et al. (2022) the CEERS v0.07 photometry catalog was produced by using SOURCE EXTRACTOR (Bertin & Arnouts 1996) v2.25.0 in two-image mode, with an inverse-variance-weighted combination of the point-spread function (PSF)–matched F277W and F356W images as the detection image, and photometry measured on all seven bands.

3. Sample Selection

For this pilot study we follow the procedure below to identify a sample of galaxies with stellar mass $M_* \geqslant 10^{10} M_\odot$ at redshifts $1 \leqslant z \leqslant 3$ that are in the multiwavelength catalogs for the Extended Groth Strip (EGS; Stefanon et al. 2017) for CANDELS (Grogin et al. 2011; Koekemoer et al. 2011) and have CEERS NIRCam imaging.

The redshift range $1 \leqslant z \leqslant 3$ was selected for the following reasons. We set an upper limit of $z \leqslant 3$ so that we can trace the rest-frame NIR light at wavelengths $\lambda \geqslant 1.1$ μm using the longest-wavelength F444W NIRCam image. We set our lower limit at $z \geqslant 1$ as most HST studies have explored bars in the rest-frame optical light out to $z \sim 1.2$ (see Section 1) and the properties of bars at $z > 1$ constitute an uncharted territory of great interest. Additionally, in the redshift range of $z \sim 1$–3, the empirically measured PSF of $0\farcs16$ in the F444W band corresponds to a high spatial resolution of ∼1.3 kpc.

The sample of galaxies is derived by crossmatching the CEERS v0.07 source catalog (Finkelstein et al. 2022) with the CANDELS EGS catalog (Stefanon et al. 2017) within $0\farcs25$ and identifying galaxies with stellar mass $M_* \geqslant 10^{10} M_\odot$ at redshifts $1 \leqslant z \leqslant 3$. At $z \sim 2$, the 90% stellar mass completeness of the CANDELS EGS catalog is $\sim 10^{10} M_\odot$ (Stefanon et al. 2017). This crossmatching results in a sample of 348 galaxies with stellar mass $M_* \geqslant 10^{10} M_\odot$ at redshifts $1 \leqslant z \leqslant 3$.

We use the robust photometric redshifts and stellar mass measurements in the value-added catalogs associated with the CANDELS EGS catalogs (Stefanon et al. 2017). For ∼67% of the sample, we supplement photometric redshifts with available published spectroscopic redshifts in EGS (N. Hathi 2022, private communication). If a source has more than one spectroscopic redshift measurement, we choose the one with the highest quality.

4. Methodology

4.1. Identification of Stellar Bars

Stellar bars are nonaxisymmetric, flattened triaxial systems within stellar disks that are made up of families of periodic stellar orbits that conserve the Jacobi integral. The main bar-supporting family of x_1 orbits are elongated along the long axis of the stellar bar (e.g., Contopoulos & Papayannopoulos 1980; Athanassoula 1992b). Our methodology to identify bars in the JWST data consists of two stages outlined below.

Stage 1: The first stage is a liberal visual classification whose goal is to cast as wide a net as possible for systems with elongated structures that may be putative bar candidates, with the idea that subsequent ellipse fits of these candidates would allow us to identify the barred systems. For the visual classification, we visually inspected postage stamps of six NIRCam images (F115W, F150W, F200W, F277W, F356W, and F444W) of our 348 sample galaxies at $1 \leqslant z \leqslant 3$ to first remove unresolved systems and very strongly distorted and asymmetric systems. Among the remaining galaxies, we then liberally selected a sample S1 of galaxies that host any elongated structures (in any band) that might even marginally be stellar bars. We ended up with 82 galaxies in sample S1.

Stage 2: The second stage involves using the methodology described in Jogee et al. (2004) and Marinova & Jogee (2007) to identify bars. In brief, this methodology involves ellipse fitting the tracer images (e.g., Jedrzejewski 1987; Wozniak et al. 1995; Jogee et al. 2002, 2004; Elmegreen et al. 2004; Marinova & Jogee 2007), followed by the application of quantitative criteria to identify bars. For this second stage, we ellipse fitted the F444W image of each galaxy in sample S1. Figure 1 illustrates the effects of bandpass shift and PSF for an example barred galaxy (EGS-23205) at redshift $z \sim 2.136$ in our sample. The stellar bar is evident in the high-resolution rest-frame NIR (JWST F444W) image, but not in the rest-frame UV (JWST F115W) image. The bar is more evident in the rest-frame NIR JWST F444W image than in the rest-frame blue optical HST F160W image although the images have a similar PSF ($0\farcs18$ and $0\farcs16$, respectively).

Before ellipse fitting the F444W images of the 82 putative barred galaxies, nearby sources were masked and the pixel

[37] https://jwst-pipeline.readthedocs.io/en/latest/

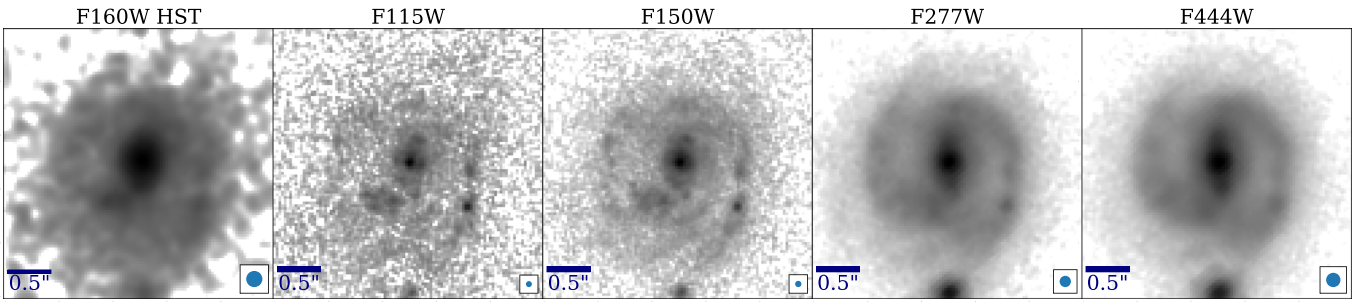

Figure 1. Effects of bandpass shift and PSF for an example barred galaxy (EGS-23205) at redshift $z \sim 2.136$ in our sample. From left to right, we show the HST WFC3 F160W and JWST NIRCam F115W, F150W, F277W, and F444W images. The blue circle at the bottom right of each image represents the point-spread function (PSF) FWHM of each band ($0\farcs18$, $0\farcs07$, $0\farcs07$, $0\farcs13$, and $0\farcs16$, respectively) and the horizontal bar shows a $0\farcs5$ scale for reference. All images are $3\farcs0 \times 3\farcs0$ in size. The underlying stellar mass distribution and galactic components, such as the stellar bar, are better traced by the high-resolution rest-frame NIR image revealed by the JWST F444W data than by the rest-frame UV light shown in the JWST F115W images. It is also striking that although the HST F160W and JWST F444W images have a similar PSF ($0\farcs18$ and $0\farcs16$, respectively), the bar is more evident in the JWST image due to the longer rest-frame wavelength light the latter is tracing. Signs of the bar are also visible in the high-resolution rest-frame red optical image traced by the JWST F227W data, but are much less evident in the rest-frame blue optical light traced by the JWST F150W image. In all images, N is up, and E is left.

values were replaced with interpolated values from the nearby region. Then, the ellipse fitting was done in two steps:

1. We ran "isophote.Ellipse.fit_image" in PHOTUTILS from Python's astropy package (Bradley et al. 2020) without fixing the center. Doing this step, we let the code fully explore the image and return the center of the ellipse for every ellipse fitted. We then determined the center of isophotes in step 2 by measuring the average center of the ellipses fitted to the inner region.
2. We fixed the center of isophotes at the center measured in step 1 and ran the same routine "isophote.Ellipse.fit_image." During the fitting, the semimajor axis grows geometrically by a factor of 1.1 for each step, and the fitting stops when the relative error in the local radial intensity gradient exceeds 0.5 (Busko 1996) for two consecutive ellipses or the outermost ellipse extends to the region with low signal-to-noise ratio ($S/N \leqslant 3$). From the ellipse fits we generate radial profiles of surface brightness (SB), ellipticity (e), and position angle (PA) plotted versus the ellipse semimajor axis a (e.g., see Figures 2 and 3).

In alignment with best practices in the study of bars, we exclude from further consideration all galaxies with large inclinations ($i > 60°$ as inferred from projected axis ratios of the outer ellipse) as the bar and the outer disk are very hard to separate in such systems. Among the remaining bar candidates, we consider a galaxy to be barred only if it satisfies the two criteria below (e.g., Jogee et al. 2004; Marinova & Jogee 2007):

1. In the bar-dominated region, we require the ellipticity e to rise smoothly to a maximum value $e_{\max} > 0.25$, while the PA stays fairly constant along the bar, with some small variation $\Delta\theta_1$ allowed. We discuss the value of $\Delta\theta_1$ later in this section.
2. In the region dominated by the outer disk, we require the ellipticity to drop by at least 0.1 from the bar's maximum ellipticity and the PA to change by at least 10° from the associated bar PA. In galaxies where a transition region exists between the end of the bar and the region dominated by the outer disk, we apply the above criterion to the outer disk region beyond it.

We refer the reader to Jogee et al. (2004) and Marinova & Jogee (2007) for a description of the physically motivated justification for the above two criteria for bar identification. We comment here further on the criteria related to the PA. In the first criterion, we required the PA to stay fairly constant along the bar, with some small variation $\Delta\theta_1$ allowed. The rationale for a relatively constant PA is that the main $\boldsymbol{x}_1$ family of bar-supporting orbits can be modeled by concentric ellipses with a fairly constant PA as a function of semimajor axis in the bar region (Athanassoula 1992b). Many studies do not specify the value they adopt for the allowed variation $\Delta\theta_1$, while others use a wide range in $\Delta\theta_1$ from 20° to 40° (e.g., Jogee et al. 2004; Marinova & Jogee 2007; Olguín-Iglesias et al. 2020). In this pilot Letter, we will only show six examples of robustly identified bar candidates where the variation $\Delta\theta_1$ of the PA along the bar is conservatively low at $\Delta\theta_1 \leqslant 20°$ (see Section 5). In our future papers that aim for a more complete census of bars at $z > 1$, we will explore the impact of adopting larger $\Delta\theta_1$ values and fine-tuning other aspects of the methodology.

Examples of ellipse fits are shown in Figures 2 and 3 and discussed in the next section. The above two criteria are quite effective in separating barred galaxies from inclined disk galaxies (e.g., see Figure A1 in the Appendix) and unbarred galaxies (e.g., see Figure A1 in the Appendix). We also note that short bars will not be identified in the JWST F444W images due to the loss of spatial resolution. We do not expect to robustly identify bars whose semimajor axis is less than the PSF of F444W images ($0\farcs16$ corresponding to ~1.3 kpc at $z \sim 1$–3).

4.2. Characterization of Bar Length and Maximum Ellipticity

The shape, length, and stellar mass of a stellar bar are important properties that determine the gravitational torque it exerts and its impact on the secular evolution of a galaxy. The main goal of this Letter is to identify and demonstrate the existence of bars at $z > 1$, and the ellipse fits presented in the previous section are adequate for this purpose as they robustly identify bars. However, for characterizing the strength, shape, and size of bars, there are more sophisticated methods than ellipse fits and in our future papers we will explore such methods, including generalized ellipses with a shape parameter (Athanassoula et al. 1990; Gadotti 2009a) and multicomponent (bulge, bar, outer disk) decomposition of the light distribution

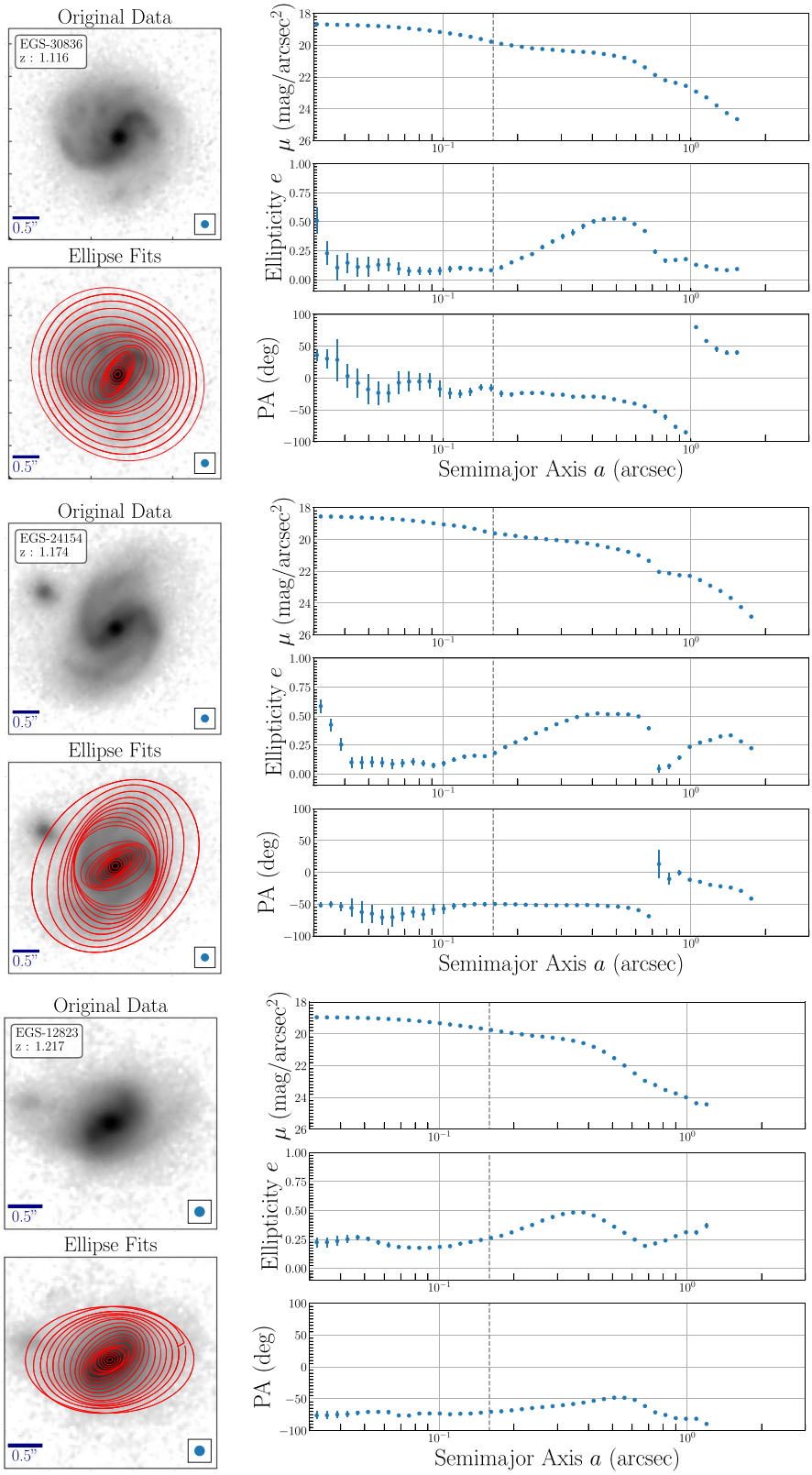

Figure 2. Ellipse fits to the JWST NIRCam F444W image of three example barred galaxies (EGS-30836, EGS-24154, and EGS-12823). The left panel for each galaxy shows the F444W image alone (top) and then with the ellipse fits superposed (bottom). Although nearby sources may appear in the images, they are masked during the ellipse fitting. The blue circle at the bottom right of each image represents the PSF FWHM ($0\farcs16$ corresponding to ∼1.3 kpc at $z \sim 1$–3), and the horizontal bar shows a $0\farcs5$ scale for reference. The size of each image is adjusted with respect to the size of the source, and ranges from $3\farcs0 \times 3\farcs0$ to $3\farcs9 \times 3\farcs9$. The right panel for each galaxy shows the radial profiles of surface brightness (μ), ellipticity (e), and position angle (PA) versus semimajor axis a derived from the ellipse fits. See Section 4.1 for details. PA goes from 0° to −90° clockwise (from N to W) and goes from 0° to 90° counterclockwise (from N to E). The vertical dashed line represents the F444W PSF ($0\farcs16$).

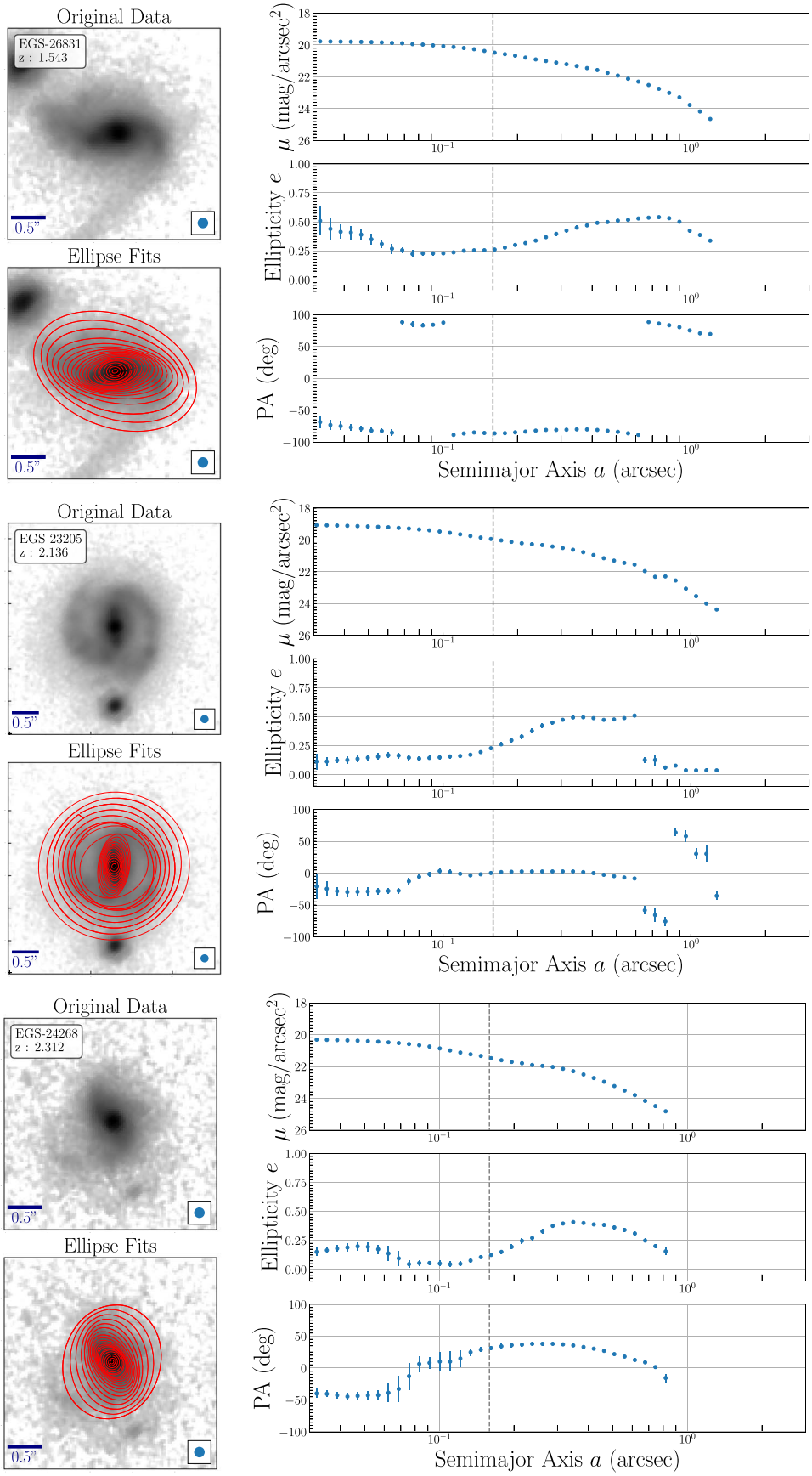

Figure 3. Same as Figure 2, but for three other example barred galaxies (EGS-26831, EGS-23205, and EGS-24268). See Section 4 for details.

Table 1
Barred Galaxies at $z > 1$ in the Rest-frame NIR from JWST

Galaxy Name	z_{spec}	e_{bar}	a_{bar} (arcsec)	a_{bar} (kpc)	$\log(M_\star/M_\odot)$	SFR ($M_\odot$ yr^{-1})
EGS-30836	1.116 (DEEP2 DR4)	∼0.53	∼0.51	∼4.28	10.80	48.430
EGS-24154	1.174 (DEEP2 DR4)	∼0.52	∼0.42	∼3.57	11.05	45.395
EGS-12823	1.217 (3D-HST)	∼0.48	∼0.38	∼3.26	10.63	21.230
EGS-26831	1.543 (MOSDEF)	∼0.49	∼0.42	∼3.65	10.40	74.290
EGS-23205	2.136 (3D-HST)	∼0.50	∼0.35	∼2.95	11.29	295.023
EGS-24268	2.312 (MOSDEF)	∼0.41	∼0.35	∼2.91	10.16	112.808

Note. Columns are as follows: (1) Galaxy ID from Stefanon et al. (2017). (2) Spectroscopic redshift and the survey on which it is based. The 3D-HST redshifts for EGS-12823 and EGS-23205 are based on grism spectra in the 3D-HST Survey (Brammer et al. 2012; Momcheva et al. 2016) and are well constrained. The DEEP2 DR4 and MOSDEF spectroscopic redshifts are from Newman et al. (2013) and Kriek et al. (2015), respectively. (3) The maximum projected ellipticity e_{bar} of the stellar bar in the rest-frame NIR based on JWST NIRCam F444W images. (4) As in column (3), but for the bar projected semimajor axis a_{bar} in arcsec. (5) As in column (3), but for the bar projected semimajor axis a_{bar} in kpc. (6) Stellar mass measurements of the host galaxy from "M_neb_med" column in Stefanon et al. (2017). (7) Star formation rate (SFR) measurements of the host galaxy are the best estimate of the total SFR from the value-added catalogs associated with the CANDELS EGS catalogs (Barro et al. 2019).

(e.g., Laurikainen et al. 2005, 2007; Gadotti 2009b; Weinzirl et al. 2009).

In this Letter, we focus on the ellipticity and length of the bar based on ellipse fits. We consider the maximum projected ellipticity of the bar e_{bar} as one measure of bar strength. In the radial profile of projected ellipticity from the ellipse fits (see Figures 2 and 3), the ellipticity rises smoothly to a maximum value in the bar-dominated region and we take this maximum value as e_{bar}.

Different definitions of the bar length are used in the bar community, including the following: (i) the semimajor axis (sma) a_{bar} where the bar ellipticity first reaches a maximum value along the bar; (ii) the sma where the bar ellipticity drops steeply or by at least 15% from its maximum value; and (iii) the sma where the PA changes from the bar to the outer disk. In this Letter we measure bar lengths based on the first definition as the latter is widely used in many studies (e.g., Athanassoula & Misiriotis2002; Jogee et al. 2004; Marinova & Jogee 2007; Menéndez-Delmestre et al. 2007) and can be unambiguously applied to many galaxies. However, some studies (e.g., Athanassoula & Misiriotis2002; Martinez-Valpuesta et al. 2006) suggest this definition can underestimate the true bar length.

5. Results

For this pilot Letter, we choose to show six examples of robustly identified barred galaxies that fulfill the following criteria: (i) They have good ellipse fits of the F444W images (Figures 2 and 3), unambiguously meet the two bar criteria in Section 4.1, and show a conservatively small variation $\Delta\theta_1 \leqslant 20°$ in the PA of ellipses fitted along the bar. As we mentioned in Section 4.1, the variation $\Delta\theta_1$ allowed for the PA along the bar could in general be higher, but we show the most conservative robust cases of bar here. (ii) The bars have moderate to high maximum projected ellipticities ($e_{bar} \sim$ 0.41–0.53) and they are well resolved with projected semimajor axes $a_{bar} \sim 0\farcs35$–$0\farcs51$ or ∼2.9–4.3 kpc (Table 1). (iii) The barred galaxies have a range of published spectroscopic redshifts (N. Hathi 2022, private communication), at $z \sim 1.116$, 1.174, 1.217, 1.543, 2.136, and 2.312 (Table 1), and include the two highest-redshift barred galaxies at $z \sim 2.136$ and 2.312, quantitatively identified and characterized to date.

The properties of the six bars and their host galaxies are shown in Figure 4 and Table 1, and the ellipse fits to their F444W images are shown in Figures 2 and 3. In the cases of EGS-30836, EGS-24154, and EGS-12823 in Figure 2, as well as EGS-26831, EGS-23205, and EGS-24268 in Figure 3, both bar criteria are well met: the ellipticity rises smoothly to a maximum in the bar-dominated region while the PA stays constant within less than 20°, and there is a significant drop in ellipticity and change in PA in the region dominated by the outer disk.

To characterize bar properties, we estimated the maximum projected ellipticity (e_{bar}) and projected bar length (a_{bar}) of the bar for each galaxy with the method described in Section 4.2. For our barred galaxies at redshifts of $z \sim 1.1$–2.3, the stellar bar has moderate to high maximum projected ellipticities (e_{bar}) in the rest-frame NIR ranging from ∼0.41 to 0.53 (Table 1). These values overlap with the range of bar projected ellipticities (0.25–0.8) seen in NIR images of $z \sim 0$ bright spirals where most (>70%) bars have $e_{bar} \geqslant 0.4$ (e.g., Marinova & Jogee 2007; Menéndez-Delmestre et al. 2007). Once we have a larger and more complete sample of bars at $z > 1$, we can evaluate whether the distribution of bar strength and ellipticity evolves down to the present day.

The projected bar length a_{bar} in the rest-frame NIR ranges from ∼2.9–4.3 kpc with angular sizes of $\sim 0\farcs35$—$0\farcs51$ (Table 1). For the barred galaxies presented in our study, a typical measurement error due to ellipse fitting of ∼0.24–0.42 kpc ($0\farcs03$–$0\farcs05$ in angular sizes) on a_{bar} is expected as one cannot measure a_{bar} values better than the step size used in ellipse fitting. The range of a_{bar} values (∼ 2.9–4.3 kpc) in these high-redshift bars overlaps with the range of stellar bar lengths (1–14 kpc) seen in NIR images of $z \sim 0$ bright spirals where most (>75%) bars have have $a_{bar} \leqslant 5$ kpc (e.g., Marinova & Jogee 2007). However, as mentioned in Section 4.2, we do not expect to robustly identify bars less than the PSF of F444W images ($0\farcs16$ corresponding to ∼1.3 kpc at $z \sim 1$–3), so short bars are going to be missed in our study. Additionally, the normalized bar length (ratio of bar length to disk length) is a more meaningful comparison than using the bar length alone, and we will compute the normalized quantities in future papers.

Our six barred galaxies at $z \sim 1.1$–2.3 have published star formation rates (SFRs) ∼21–295 $M_\odot$ yr^{-1} (Table 1; Barro et al. 2019). The corresponding specific SFR is $\sim 4 \times 10^{-10}$ to

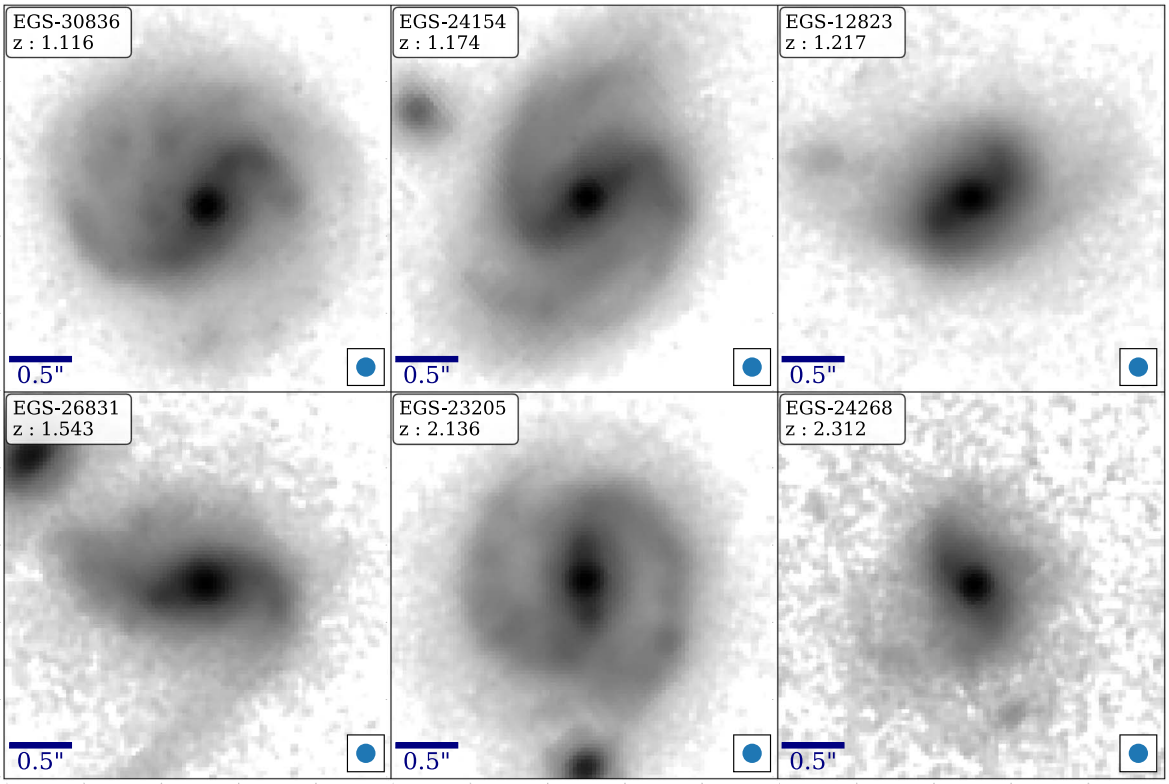

Figure 4. Montage of JWST F444W images showing the rest-frame NIR morphology of the six example barred galaxies presented in this Letter. The bars were identified by applying quantitative criteria to ellipse fits as outlined in Section 4. The labels in the top left of each figure show the CANDELS ID and redshift of each galaxy. The galaxies have spectroscopic redshifts of 1.116, 1.174, 1.217, 1.543, 2.136, and 2.312, and the last two cases represent the highest-redshift bars quantitatively identified and characterized to date. The blue circle at the bottom right of each image represents the point-spread function (PSF) FWHM ($0\farcs16$ corresponding to $\sim$1.3 kpc at $z\sim2$), and the horizontal bar shows a $0\farcs5$ scale for reference. All images are $3\farcs0\times3\farcs0$ in size.

8×10^{-9} yr^{-1}, indicating these systems are actively star forming. We stress that this result only applies to the subset of bars we present here and a wider range of specific SFRs may be present in the full bar population.

Our pilot study of barred galaxies at $z>1$ using high-resolution rest-frame NIR images from JWST complements the many past studies that have used HST data to explore bars in the rest-frame optical out to $z\sim1.2$ (e.g., Elmegreen et al. 2004; Jogee et al. 2004; Sheth et al. 2008; Cameron et al. 2010; Melvin et al. 2014) and out to $z\leqslant2.0$ (Simmons et al. 2014).

Our study also complements several other recent JWST studies that have been submitted or recently accepted for publication. Jacobs et al. (2022) explore the rest-frame optical morphologies of galaxies at $0.8<z<5.4$ through visual classification of JWST data, mentioning that "several sources additionally show distinct bars," but provide no further information on the barred galaxies. Chen et al. (2022) perform two-dimensional surface brightness profile fittings of JWST images to explore bulges in $z\sim2$ submillimeter galaxies (Zavala et al. 2017, 2018) and mentions an additional bar component is also needed to improve the fit for EGS-23205 (source 850.025). Finally, Ferreira et al. (2022a) explore morphologies of galaxies at $1.5<z<8$ through visual classification of JWST images and focus on disks, spheroids, and peculiar galaxies. They mention in some cases, such as our galaxy EGS-23205, "a disk, spiral arms and a bar pops up in the longer wavelength bands," but they do not present a further analysis of the bar. Our study complements the above studies by using quantitative criteria based on ellipse fits of rest-frame JWST NIR images to identify bars and to characterize their properties (lengths, ellipticities) and that of their host galaxies. To the best of our knowledge, the two barred galaxies in our pilot study with spectroscopic redshifts $z\sim2.136$ and $z\sim2.312$ are the highest-redshift bars quantitatively identified and characterized to date.

6. Discussion

When discussing our results, it is important to bear in mind that our pilot study does not present a full census of bars and, instead, only highlights six examples of bars at $z>1$, which have been quantitatively identified and include the two highest-redshift bars at $z\sim2.136$ and 2.312 known to date. Nonetheless, our present results already allow some interesting conclusions to be drawn and open up exciting possibilities for future work.

Our finding of well developed bars at $z\sim1.1$–2.3 with projected semimajor axes of $\sim$2.9–4.3 kpc and and projected maximum ellipticities of $\sim$0.41–0.53 in the rest-frame NIR (Section 5) demonstrates the early onset of such features and supports simulations where bars form early in massive dynamically cold disks (e.g., Bournaud & Combes 2002; Romano-Díaz et al. 2008; Kraljic et al. 2012; Bonoli et al. 2016; Spinoso et al. 2017; Bi et al. 2022; Rosas-Guevara et al. 2022). In a future paper, we will present a census of observable bars at $z>1$ and estimate the bar fraction in the rest-frame NIR out to $z\sim3$ using F444W images. These images will detect obscured bars, but the F444W PSF ($0\farcs16$ or $\sim$1.3 kpc at $z\sim1$–3) will only allow the robust identification of bars with length above 1.3 kpc at $z\sim1$–3. We will also estimate the

rest-frame optical bar fraction out $z \sim 4$ using F200W and other images. While the rest-frame optical images may miss bars impacted by dust and SF, their smaller PSF (0.″08 or ∼650 pc at $z \sim 1$–3) allows them to detect shorter subkiloparsec bars, which may constitute a significant fraction of the bars in disk galaxies at early epochs (e.g., Rosas-Guevara et al. 2020, 2022). Recent studies in the rest-frame optical identify a large fraction of disk galaxies at $z \sim 3$ in JWST data (e.g., Ferreira et al. 2022b; Kartaltepe et al. 2022).

The topic of the formation, lifetime, and evolution of bars is an area of active research and it depends on the interplay between the stellar disk, dark matter halo, and gaseous components. The properties of the dark matter halo and its exchange of angular momentum with stellar or gaseous components impact the bar (e.g., Athanassoula 2003; Athanassoula et al. 2013; Saha & Naab 2013; Sellwood 2016; Collier et al. 2018; Beane et al. 2022). The role of gas is complex. While the presence of a massive and dynamically cold disk of stars and gas favors the onset of $m = 2$ bar instabilities (e.g., Bournaud & Combes 2002; Romano-Díaz et al. 2008; Kraljic et al. 2012; Bonoli et al. 2016; Spinoso et al. 2017; Bi et al. 2022; Rosas-Guevara et al. 2022), gas clumps that sink by dynamical friction can heat the stellar disk (e.g., Shlosman & Noguchi 1993), and large central gaseous mass concentrations can weaken or destroy some bars (e.g., Bournaud & Combes 2002; Shen & Sellwood 2004; Athanassoula et al. 2005; Bournaud et al. 2005; Debattista et al. 2006).

Numerous simulations have also shown that bars can form spontaneously in isolated disks or be tidally induced (e.g., Hernquist & Mihos 1995; Izquierdo-Villalba et al. 2022). In that context, it is interesting to note that many of the six example barred galaxies appear to have nearby sources that could be potential companions. EGS-26831 has a spectroscopic redshift of $z \sim 1.543$ and has two potential companions detected in Stefanon et al. (2017): the source to its northeast (partially visible in Figure 4) has a similar but poorly constrained photometric redshift (Stefanon et al. 2017) within $\Delta z/(1+z) \sim 0.065$ and is at an angular distance of ∼1.″62 (corresponding to ∼14 kpc assuming for $z \sim 1.543$), while the source to the southeast (not visible in Figure 4) has a poorly constrained photometric redshift (Stefanon et al. 2017) within $\Delta z/(1+z) \sim 0.0056$ and is at an angular distance ∼ 2.″44 (corresponding to ∼ 21 kpc for $z \sim 1.543$). Even though those two sources have poorly constrained photometric redshifts, the interacting features shown in the F444W image suggest that the sources could potentially be companions of EGS-26831. For EGS-24154 whose spectroscopic redshift is $z \sim 1.174$, the source to its northeast (partially visible in Figure 4) is detected in Stefanon et al. (2017) and could be a potential companion as it has a spectroscopic redshift (3D-HST; Brammer et al. 2012; Momcheva et al. 2016) within $\Delta z/(1+z) \sim 0.001$ at an angular distance ∼ 1.″4 (corresponding to ∼12 kpc for $z \sim 1.174$). For EGS-23205 at $z \sim 2.136$, the bright source to its south (shown in Figure 4) is identified as an X-ray-luminous AGN with an estimated photometric redshift of $z \sim 4.1$ (Kocevski et al. 2022). Given the difficulty of deriving accurate photometric redshifts for luminous AGN, it is unclear how reliable this redshift is and whether the AGN is a chance projection or a true companion. It is also noteworthy that there are faint sources near EGS-30836, EGS-12823, and EGS-24268. Those faint sources are not detected in the CANDELS EGS catalog (Stefanon et al. 2017), so we do not have redshifts to determine whether they are companions, accreted sources, or overdensities in the disk. In future papers we will explore the frequency of tidal interactions in a larger sample of barred galaxies and a control sample of unbarred systems.

The growth and rich morphological transformation of galaxies from $z \sim 4$ to today is likely driven by several mechanisms, including bar-driven secular processes (e.g., Sakamoto et al. 1999; Kormendy & Kennicutt 2004; Jogee et al. 2005), galaxy mergers and tidal interactions (e.g., Conselice et al. 2003; Kartaltepe et al. 2007; Jogee et al. 2009; Lotz et al. 2010), and gas accretion (e.g., Katz et al. 2003; Kereš et al. 2005; Dekel & Birnboim 2006; Faucher-Giguère & Keres 2011; Kereš et al. 2012). Our finding of bars at $z \sim 1.1$–2.3 (lookback times of 8–11 Gyr) also suggests that if these bars survive out to present epochs, bar-driven secular processes may operate over a long time and have a significant impact on some galaxies by $z \sim 0$. In this context, we note that Gadotti et al. (2015) suggest that the bar in the nearby galaxy NGC 4371 has a formation epoch of $z \sim 2$.

Our subset of barred galaxies at at $z \sim 1.1$–2.3 have SFRs ∼21–295 $M_\odot$ yr^{-1} and specific SFRs $\sim 4 \times 10^{-10}$–8×10^{-9} yr^{-1} and are thus actively forming stars. Bars drive large gas inflows into the circumnuclear regions via gravitational torques and shocks and can lead a phase of high circumnuclear SFR and potentially depressed or quenched SF in the disk (e.g., Hunt & Malkan 1999; Jogee et al. 2005; Masters et al. 2010, 2012; Khoperskov et al. 2018; George et al. 2021). We will explore more fully the impact of bars on galaxy SFRs in a future paper where we will incorporate the upcoming additional CEERS pointings and make a statistical comparison of the SFRs of barred and unbarred systems.

7. Summary

The exploration of stellar bars out to early cosmic times is essential for understanding the evolution of galaxies as bars play a critical role in driving the secular evolution of galaxies. Stellar bars can be effectively mapped in rest-frame NIR images, which trace the underlying stellar mass and are less impacted by dust and star formation than rest-frame UV or optical images. In this pilot study we conduct the first quantitative identification and characterization of stellar bars at $z > 1$ in high-resolution rest-frame NIR images by analyzing JWST F444W images in the first epoch of imaging from the CEERS survey. We focus on a sample of 348 galaxies at redshifts $1 \leqslant z \leqslant 3$, with stellar mass $M_* \geqslant 10^{10} M_\odot$ and CANDELS multiwavelength data.

The JWST F444W images allow us to achieve a high-resolution (0.″16 corresponding to ∼1.3 kpc at $z \sim 1$–3) at rest-frame NIR wavelengths to quantitatively identify and characterize bars at $z > 1$. We identify stellar bars by performing a first-pass visual classification, followed by ellipse fits and the application of physically motivated quantitative criteria to the ellipse fits. For this pilot study we present six examples of robustly identified bars at $z > 1$ with spectroscopic redshifts, including the two highest-redshift bars at $z \sim 2.136$ and 2.312, quantitatively identified and characterized to date. Our study complements HST studies in the past two decades that have mainly traced bars in the rest-frame optical out to $z \sim 1$.

The examples of stellar bars at $z \sim 1.1$–2.3 presented in our study have projected semimajor axes of ∼2.9–4.3 kpc and moderate to high projected maximum ellipticities of ∼0.41–0.53 in the rest-frame NIR, indicating they are already fairly strong and well developed at these early cosmic times. The barred host galaxies have stellar masses

$\sim 1 \times 10^{10}$–2×10^{11} $M_{\odot}$, star formation rates of ∼21–295 $M_{\odot}$ yr^{-1}, and several have potential nearby companions. Our finding of bars at $z \sim 1.1$–2.3 demonstrates the early onset of such instabilities and supports simulations where bars form early in massive dynamically cold disks. It also suggests that if these bars at lookback times of 8–11 Gyr survive out to present epochs, bar-driven secular processes may operate over a long time and have a significant impact on some galaxies by $z \sim 0$.

This pilot study only presents six examples of robustly identified bars at $z > 1$ in the rest-frame NIR. We do not present here a full census of all observable bars at $z > 1$ and the associated statistical distribution of their properties. In future papers that will incorporate the upcoming additional six CEERS pointings, we will present such a census, estimate the rest-frame optical and NIR bar fraction, and explore the relationship between bars and galaxy properties (SF, bulges, AGN, and the presence of companions) using a control sample of unbarred galaxies.

Version v0.07 of the CEERS data reduction was used in this work. The full set of the latest CEERS data products can be found at MAST via doi:10.17909/z7p0-8481.

We thank the entire JWST team, including the engineers for making possible this wonderful overperforming telescope, the commissioning team for obtaining these early data, and the pipeline teams for their work over the years building and supporting the pipeline. Y.G. and S.J. acknowledge support from the Roland K. Blumberg Endowment in Astronomy and Heising-Simons Foundation grant 2017-0464. M.B.B. and S.L. F. acknowledge support from NASA through STScI ERS award JWST-ERS-1345. The authors acknowledge the Texas Advanced Computing Center (TACC) at The University of Texas at Austin for providing HPC and visualization resources that have contributed to the research results reported within this paper (http://www.tacc.utexas.edu).

Software: `Astropy` (Astropy Collaboration et al. 2013), `Photutils` (Bradley et al. 2020), `SciPy` (Virtanen et al. 2020), `Source Extractor` (Bertin & Arnouts 1996), `STScI` JWST Calibration Pipeline (https://jwst-pipeline.readthedocs.io/en/latest/).

Appendix

In Section 4.1, we describe our criteria for identifying barred galaxies from the radial profiles of surface brightness, ellipticity and position angle. Here we illustrate that these criteria are effective in separating barred galaxies from unbarred galaxies (e.g., see Figure A1, top panel) and inclined disk galaxies (e.g., see Figure A1, bottom panel).

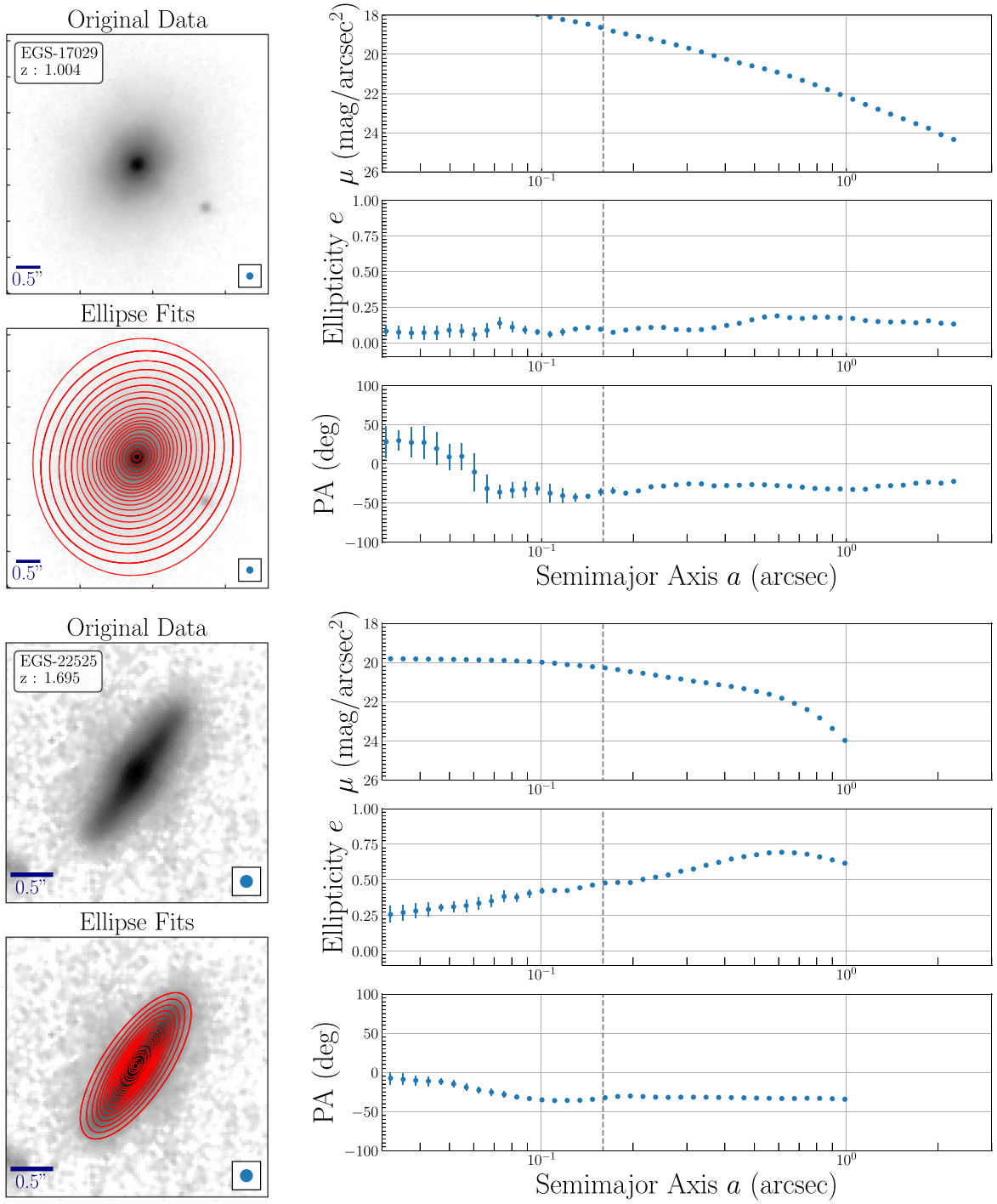

Figure A1. Ellipse fits to the JWST NIRCam F444W image of an unbarred face-on disk galaxy (EGS-17029) and an inclined disk galaxy (EGS-22525). The left panel for each galaxy shows the F444W image alone (top) and then with the ellipse fits superposed (bottom). The blue circle at the bottom right of each image represents the PSF FWHM (0.″16 corresponding to ∼1.3 kpc at $z \sim 1$–3), and the horizontal bar shows a 0.″5 scale for reference. The size of each image is adjusted with respect to the size of the source, and ranges from 4.″5 × 4.″5 to 3.″0 × 3.″0. The right panel for each galaxy shows the radial profiles of surface brightness (μ), ellipticity (e), and position angle (PA) versus semimajor axis a derived from the ellipse fits. The vertical dashed line represents the F444W PSF (0.″16). The profiles do not show the characteristic signatures that meet our bar criteria in Section 4.1.

ORCID iDs

Yuchen Guo https://orcid.org/0000-0002-4162-6523
Shardha Jogee https://orcid.org/0000-0002-1590-0568
Steven L. Finkelstein https://orcid.org/0000-0001-8519-1130
Micaela B. Bagley https://orcid.org/0000-0002-9921-9218
Guillermo Barro https://orcid.org/0000-0001-6813-875X
Stijn Wuyts https://orcid.org/0000-0003-3735-1931
Dale D. Kocevski https://orcid.org/0000-0002-8360-3880
Jeyhan S. Kartaltepe https://orcid.org/0000-0001-9187-3605
Elizabeth J. McGrath https://orcid.org/0000-0001-8688-2443
Henry C. Ferguson https://orcid.org/0000-0001-7113-2738

Bahram Mobasher https://orcid.org/0000-0001-5846-4404
Mauro Giavalisco https://orcid.org/0000-0002-7831-8751
Ray A. Lucas https://orcid.org/0000-0003-1581-7825
Jorge A. Zavala https://orcid.org/0000-0002-7051-1100
Jennifer M. Lotz https://orcid.org/0000-0003-3130-5643
Norman A. Grogin https://orcid.org/0000-0001-9440-8872
Marc Huertas-Company https://orcid.org/0000-0002-1416-8483
Jesús Vega-Ferrero https://orcid.org/0000-0003-2338-5567
Nimish P. Hathi https://orcid.org/0000-0001-6145-5090
Pablo Arrabal Haro https://orcid.org/0000-0002-7959-8783
Mark Dickinson https://orcid.org/0000-0001-5414-5131
Anton M. Koekemoer https://orcid.org/0000-0002-6610-2048
Casey Papovich https://orcid.org/0000-0001-7503-8482
Nor Pirzkal https://orcid.org/0000-0003-3382-5941
L. Y. Aaron Yung https://orcid.org/0000-0003-3466-035X
Bren E. Backhaus https://orcid.org/0000-0001-8534-7502
Eric F. Bell https://orcid.org/0000-0002-5564-9873
Antonello Calabrò https://orcid.org/0000-0003-2536-1614
Nikko J. Cleri https://orcid.org/0000-0001-7151-009X
Rosemary T. Coogan https://orcid.org/0000-0002-4343-0479
M. C. Cooper https://orcid.org/0000-0003-1371-6019
Luca Costantin https://orcid.org/0000-0001-6820-0015
Darren Croton https://orcid.org/0000-0002-5009-512X
Kelcey Davis https://orcid.org/0000-0001-8047-8351
Avishai Dekel https://orcid.org/0000-0003-4174-0374
Maximilien Franco https://orcid.org/0000-0002-3560-8599
Jonathan P. Gardner https://orcid.org/0000-0003-2098-9568
Benne W. Holwerda https://orcid.org/0000-0002-4884-6756
Taylor A. Hutchison https://orcid.org/0000-0001-6251-4988
Viraj Pandya https://orcid.org/0000-0002-2499-9205
Pablo G. Pérez-González https://orcid.org/0000-0003-4528-5639
Swara Ravindranath https://orcid.org/0000-0002-5269-6527
Caitlin Rose https://orcid.org/0000-0002-8018-3219
Jonathan R. Trump https://orcid.org/0000-0002-1410-0470
Alexander de la Vega https://orcid.org/0000-0002-6219-5558
Weichen Wang https://orcid.org/0000-0002-9593-8274

References

Abraham, R. G., Merrifield, M. R., Ellis, R. S., Tanvir, N. R., & Brinchmann, J. 1999, MNRAS, 308, 569
Algorry, D. G., Navarro, J. F., Abadi, M. G., et al. 2017, MNRAS, 469, 1054
Astropy Collaboration, Robitaille, T. P., Tollerud, E. J., et al. 2013, A&A, 558, A33
Athanassoula, E. 1992a, MNRAS, 259, 345
Athanassoula, E. 1992b, MNRAS, 259, 328
Athanassoula, E. 2002, ApJL, 569, L83
Athanassoula, E. 2003, MNRAS, 341, 1179
Athanassoula, E. 2005, MNRAS, 358, 1477
Athanassoula, E., Machado, R. E. G., & Rodionov, S. A. 2013, MNRAS, 429, 1949
Athanassoula, E., & Misiriotis, A. 2002, MNRAS, 330, 35
Athanassoula, E., Morin, S., Wozniak, H., et al. 1990, MNRAS, 245, 130
Bagley, M. B., Finkelstein, S. L., Koekemoer, A. M., et al. 2022, ApJ, submitted, arXiv:2211.02495
Barro, G., Pérez-González, P. G., Cava, A., et al. 2019, ApJS, 243, 22
Beane, A., Hernquist, L., D'Onghia, E., et al. 2022, MNRAS, submitted, arXiv:2209.03364
Bertin, E., & Arnouts, S. 1996, A&AS, 117, 393
Bi, D., Shlosman, I., & Romano-Díaz, E. 2022, ApJ, 934, 52
Binney, J., Gerhard, O. E., Stark, A. A., Bally, J., & Uchida, K. I. 1991, MNRAS, 252, 210
Blitz, L., & Spergel, D. N. 1991, ApJ, 379, 631
Bonoli, S., Mayer, L., Kazantzidis, S., et al. 2016, MNRAS, 459, 2603
Bournaud, F., & Combes, F. 2002, A&A, 392, 83
Bournaud, F., Combes, F., & Semelin, B. 2005, MNRAS, 364, L18
Bradley, L., Sipőcz, B., Robitaille, T., et al. 2020, astropy/photutils: v1.0.0, Zenodo, doi:10.5281/zenodo.4044744
Brammer, G. B., van Dokkum, P. G., Franx, M., et al. 2012, ApJS, 200, 13
Busko, I. C. 1996, in ASP Conf. Ser. 101, Astronomical Data Analysis Software and Systems V, ed. G. H. Jacoby & J. Barnes (San Francisco, CA: ASP), 139
Buta, R., & Combes, F. 1996, FCPh, 17, 95
Cameron, E., Carollo, C. M., Oesch, P., et al. 2010, MNRAS, 409, 346
Casertano, S., de Mello, D., Dickinson, M., et al. 2000, AJ, 120, 2747
Chen, C.-C., Gao, Z.-K., Hsu, Q.-N., et al. 2022, ApJL, 939, L7
Collier, A., Shlosman, I., & Heller, C. 2018, MNRAS, 476, 1331
Combes, F., & Gerin, M. 1985, A&A, 150, 327
Conselice, C. J., Bershady, M. A., Dickinson, M., & Papovich, C. 2003, AJ, 126, 1183
Contopoulos, G., & Papayannopoulos, T. 1980, A&A, 92, 33
Debattista, V. P., Mayer, L., Carollo, C. M., et al. 2006, ApJ, 645, 209
Dekel, A., & Birnboim, Y. 2006, MNRAS, 368, 2
Elmegreen, B. G., Elmegreen, D. M., & Hirst, A. C. 2004, ApJ, 612, 191
Eskridge, P. B., Frogel, J. A., Pogge, R. W., et al. 2000, AJ, 119, 536
Faucher-Giguère, C.-A., & Kereš, D. 2011, MNRAS, 412, L118
Ferreira, L., Adams, N., Conselice, C. J., et al. 2022b, ApJL, 938, L2
Ferreira, L., Conselice, C. J., Sazonova, E., et al. 2022a, ApJ, submitted, arXiv:2210.01110
Finkelstein, S. L., Bagley, M. B., Arrabal Haro, P., et al. 2022, ApJL, 940, L55
Fragkoudi, F., Grand, R. J. J., Pakmor, R., et al. 2021, A&A, 650, L16
Frogel, J. A., Quillen, A. C., & Pogge, R. W. 1996, in New extragalactic perspectives in the New South Africa, Proc. of the int. conf. on "Cold Dust and Galaxy Morphology" 209, ed. D. L. Block & J. M. Greenberg (Dordrecht: Springer), 65
Fruchter, A. S., & Hook, R. N. 2002, PASP, 114, 144
Gadotti, D. A. 2009a, in Astrophysics and Space Science Proc., Chaos in Astronomy, 8 (Berlin: Springer),159
Gadotti, D. A. 2009b, MNRAS, 393, 1531
Gadotti, D. A. 2011, MNRAS, 415, 3308
Gadotti, D. A., Seidel, M. K., Sánchez-Blázquez, P., et al. 2015, A&A, 584, A90
Gardner, J. P., Mather, J. C., Clampin, M., et al. 2006, SSRv, 123, 485
George, K., Subramanian, S., Clampin, M., et al. 2021, A&A, 651, A107
Grogin, N. A., Kocevski, D. D., Faber, S. M., et al. 2011, ApJS, 197, 35
Hernquist, L., & Mihos, J. C. 1995, ApJ, 448, 41
Hunt, L. K., & Malkan, M. A. 1999, ApJ, 516, 660
Izquierdo-Villalba, D., Bonoli, S., Rosas-Guevara, Y., et al. 2022, MNRAS, 514, 1006
Jacobs, C., Glazebrook, K., Calabrò, A., et al. 2022, ApJL, submitted, arXiv:2208.06516
Jedrzejewski, R. I. 1987, MNRAS, 226, 747
Jogee, S. 2006, in Physics of Active Galactic Nuclei at all Scales, ed. D. Alloin, R. Johnson, & P. Lira, Vol. 693 (Berlin: Springer), 143
Jogee, S., Barazza, F. D., Rix, H.-W., et al. 2004, ApJL, 615, L105
Jogee, S., Knapen, J. H., Laine, S., et al. 2002, ApJL, 570, L55
Jogee, S., Miller, S. H., Penner, K., et al. 2009, ApJ, 697, 1971
Jogee, S., Scoville, N., & Kenney, J. D. P. 2005, ApJ, 630, 837
Kartaltepe, J. S., Rose, C., Vanderhoof, B. N., et al. 2022, ApJL, in press, arXiv:2210.14713
Kartaltepe, J. S., Sanders, D. B., Scoville, N. Z., et al. 2007, ApJS, 172, 320
Katz, N., Keres, D., Dave, R., & Weinberg, D. H. 2003, in Astrophysics and Space Science Library, The IGM/Galaxy Connection. The Distribution of Baryons at z = 0, 281, ed. J. L. Rosenberg & M. E. Putman (Dordrecht: Kluwer),185
Kereš, D., Katz, N., Weinberg, D. H., & Davé, R. 2005, MNRAS, 363, 2
Kereš, D., Vogelsberger, M., Sijacki, D., Springel, V., & Hernquist, L. 2012, MNRAS, 425, 2027
Khoperskov, S., Haywood, M., Di Matteo, P., Lehnert, M. D., & Combes, F. 2018, A&A, 609, A60
Knapen, J. H., Beckman, J. E., Heller, C. H., Shlosman, I., & de Jong, R. S. 1995, ApJ, 454, 623

Kocevski, D. D., Barro, G., McGrath, E. J., et al. 2022, ApJ, in press, arXiv:2208.14480
Koekemoer, A. M., Faber, S. M., Ferguson, H. C., et al. 2011, ApJS, 197, 36
Kormendy, J., & Kennicutt, R. C., Jr. 2004, ARA&A, 42, 603
Kraljic, K., Bournaud, F., & Martig, M. 2012, ApJ, 757, 60
Kriek, M., Shapley, A. E., Reddy, N. A., et al. 2015, ApJS, 218, 15
Laurikainen, E., Salo, H., Buta, R., & Vasylyev, S. 2004, MNRAS, 355, 1251
Laurikainen, E., Salo, H., & Buta, R. 2005, MNRAS, 362, 1319
Laurikainen, E., Salo, H., Buta, R., & Knapen, J. H. 2007, MNRAS, 381, 401
Lotz, J. M., Jonsson, P., Cox, T. J., & Primack, J. R. 2010, MNRAS, 404, 590
Marinova, I., & Jogee, S. 2007, ApJ, 659, 1176
Martinez-Valpuesta, I., Shlosman, I., & Heller, C. 2006, ApJ, 637, 214
Masters, K. L., Mosleh, M., Romer, A. K., et al. 2010, MNRAS, 405, 783
Masters, K. L., Nichol, R. C., Haynes, M. P., et al. 2012, MNRAS, 424, 2180
Melvin, T., Masters, K., Lintott, C., et al. 2014, MNRAS, 438, 2882
Menéndez-Delmestre, K., Sheth, K., Schinnerer, E., Jarrett, T. H., & Scoville, N. Z. 2007, ApJ, 657, 790
Momcheva, I. G., Brammer, G. B., van Dokkum, P. G., et al. 2016, ApJS, 225, 27
Newman, J. A., Cooper, M. C., Davis, M., et al. 2013, ApJS, 208, 5
Oke, J. B., & Gunn, J. E. 1983, ApJ, 266, 713
Olguín-Iglesias, A., Kotilainen, J., & Chavushyan, V. 2020, MNRAS, 492, 1450
Petters, W. L. I. 1975, ApJ, 195, 617
Planck Collaboration, Aghanim, N., Akrami, Y., et al. 2020, A&A, 641, A6
Regan, M. W., Vogel, S. N., & Teuben, P. J. 1997, ApJL, 482, L143
Romano-Díaz, E., Shlosman, I., Heller, C., & Hoffman, Y. 2008, ApJL, 687, L13
Rosas-Guevara, Y., Bonoli, S., Dotti, M., et al. 2020, MNRAS, 491, 2547
Rosas-Guevara, Y., Bonoli, S., Dotti, M., et al. 2022, MNRAS, 512, 5339
Saha, K., & Naab, T. 2013, MNRAS, 434, 1287
Sakamoto, K., Okumura, S. K., Ishizuki, S., & Scoville, N. Z. 1999, ApJ, 525, 691
Scannapieco, C., & Athanassoula, E. 2012, MNRAS, 425, L10
Schneider, P. 2006, Extragalactic Astronomy and Cosmology (Berlin: Springer)
Sellwood, J. A. 2016, ApJ, 819, 92
Shen, J., & Sellwood, J. A. 2004, ApJ, 604, 614
Sheth, K., Elmegreen, D. M., Elmegreen, B. G., et al. 2008, ApJ, 675, 1141
Shlosman, I., & Noguchi, M. 1993, ApJ, 414, 474
Simmons, B. D., Melvin, T., Lintott, C., et al. 2014, MNRAS, 445, 3466
Spinoso, D., Bonoli, S., Dotti, M., et al. 2017, MNRAS, 465, 3729
Stefanon, M., Yan, H., Mobasher, B., et al. 2017, ApJS, 229, 32
Suess, K. A., Bezanson, R., Nelson, E. J., et al. 2022, ApJL, 937, L33
Virtanen, P., Gommers, R., Oliphant, T. E., et al. 2020, NatMe, 17, 261
Weiland, J. L., Arendt, R. G., Berriman, G. B., et al. 1994, ApJL, 425, L81
Weinzirl, T., Jogee, S., Khochfar, S., Burkert, A., & Kormendy, J. 2009, ApJ, 696, 411
Wozniak, H., Friedli, D., Martinet, L., Martin, P., & Bratschi, P. 1995, A&AS, 111, 115
Zavala, J. A., Aretxaga, I., Dunlop, J. S., et al. 2018, MNRAS, 475, 5585
Zavala, J. A., Aretxaga, I., Geach, J. E., et al. 2017, MNRAS, 464, 3369